Available online at www.sciencedirect.com
SCIENCE DIRECT®
Journal of Computational Physics 209 (2005) 406–420
JOURNAL OF COMPUTATIONAL PHYSICS
www.elsevier.com/locate/jcp

MEP: A 3D PIC code for the simulation of the dynamics of a non-neutral plasma

Yu. Tsidulko [a], R. Pozzoli [b], M. Romé [b,*]

[a] *Budker Institute of Nuclear Physics, Lavrentiev Av. 11, Novosibirsk 630090, Russian Federation*
[b] *I.N.F.M., I.N.F.N., Dipartimento di Fisica, Università degli Studi di Milano, Via Celoria 16, 20133 Milano, Italy*

Received 22 April 2004; received in revised form 8 March 2005; accepted 9 March 2005
Available online 2 June 2005

Abstract

The three-dimensional evolution of a pure electron plasma is studied by means of a newly developed particle-in-cell code which solves the drift-Poisson system where kinetic effects in the motion parallel to the magnetic field are taken into account. Different results relevant to the non-linear dynamics of trapped plasmas and low-energy electron beams are presented.

PACS: 65N99; 76M28; 82D10

Keywords: Particle-in-cell; Non-neutral plasmas; Beams

1. Introduction

Single-species plasmas can be confined in Malmberg–Penning traps, where electrostatic fields are applied to a set of aligned cylindrical conductors immersed in a uniform magnetic field directed along the axis of the trap [1,2]. In this paper, we explicitly refer to electron plasmas: the plasma can be trapped in the device for a long-time, exhibit typical features of two-dimensional (2D) non-linear fluid motion (e.g. vortex merger [3,4]) and give rise to the formation of long-lasting coherent structures (vortex crystals [5]), as it approaches thermodynamic equilibrium [6]. This behavior is justified on the basis of the equivalence of the axially averaged drift-Poisson system, which describes the electron plasma, with the 2D Euler equation for an inviscid

* Corresponding author. Tel.: +39 0250317665; fax: +39 0250317205.
E-mail address: rome@mi.infn.it (M. Romé).

0021-9991/$ - see front matter © 2005 Elsevier Inc. All rights reserved.
doi:10.1016/j.jcp.2005.03.013

fluid in the limit $v_\parallel/L \gg \omega_p^2/2\omega_c$ [7], where L is the length of the longitudinal potential well, $v_\parallel$ the average parallel velocity of the electrons, $\omega_p = (4\pi e^2 n_0/m)^{1/2}$ the average plasma frequency (computed for a typical density n_0), and $\omega_c = eB/mc$ the electron cyclotron frequency in the externally applied magnetic field $\mathbf{B} = B\mathbf{e}_z$, m and $-e$ being the electron mass and charge, respectively, and $\mathbf{e}_z$ the unit vector in the z-direction (along the axis of the trap). Three-dimensional (3D) effects can be of some relevance when the above condition is not strictly satisfied [8].

A different plasma condition of interest can be considered, where a low-energy electron beam flows in the system: the electrons are continuously emitted from the cathode and collected to the anode. In this case, formation of structures and relevant phenomena can develop during the time spent by a single electron in the device, i.e., $L/v_\parallel$, where L represents in this case the length of the beam (the distance between the accelerating grid and the collector). The non-linear dynamics of the space-charge-limited flow [9] is strongly affected by the presence of the axial magnetic field: when reflection occurs in the central part of the beam a hollow electron column forms and fast coherent structures arise [10], possibly due to the development of diocotron instability.

Many phenomena related to the mentioned complex behavior both of trapped plasmas and beams can be described in the framework of the zeroth order drift approximation. In low density pure electron plasmas confined in Malmberg–Penning traps the characteristic plasma azimuthal rotation frequency ω_r is in fact typically much larger than the electron–electron collision frequency and much smaller than the plasma frequency [11],

$$\frac{\omega_r}{\omega_p} \simeq \frac{\omega_p}{2\omega_c} \ll 1. \tag{1}$$

In addition, the characteristic rotation velocity, v_θ, is much smaller than c,

$$\frac{v_\theta}{c} \simeq \frac{r_p\omega_p^2}{2c\omega_c} = \frac{r_p}{2d_e}\frac{\omega_p}{\omega_c} \ll 1. \tag{2}$$

Here, $d_e = c/\omega_p$ is the electron skin depth and r_p is the radius of the plasma column. In this regime, a purely electrostatic description of the plasma dynamics can be adopted, with the electric field given by $\mathbf{E} = -\nabla\varphi$, and the motion of the particle gyrocenters can be described in terms of the particle drift equations. To leading order in the ratio $(\omega_r/\omega_c)^2$, and assuming the externally imposed magnetic field to be spatially homogeneous, the gyrocenter motion is simply given by

$$\dot{\mathbf{x}} = \mathbf{v}_E + v_\parallel\mathbf{e}_z, \quad \dot{v_\parallel} = \frac{e}{m}\mathbf{e}_z\cdot\nabla\varphi, \tag{3}$$

where $\mathbf{v}_E \equiv (c/B)\mathbf{e}_z\times\nabla\varphi$ is the $\mathbf{E}\times\mathbf{B}$-drift velocity. Then the gyro-averaged Vlasov equation reduces to the drift kinetic equation:

$$\frac{\partial f}{\partial t} + \dot{\mathbf{x}}\cdot\nabla f + \dot{v}_\parallel\frac{\partial f}{\partial v_\parallel} = 0; \quad \nabla^2\varphi = 4\pi en, \tag{4}$$

$$n = \frac{B}{m}\int \mathrm{d}\mu\,\mathrm{d}v_\parallel f(\mathbf{x},\mu,v_\parallel,t), \tag{5}$$

where $f = f(\mathbf{x},\mu,v_\parallel,t)$ is the distribution function of the guiding centers and $\mu \equiv mv_\perp^2/2B$ is the magnetic moment with $v_\perp$ the perpendicular velocity.

Neglecting temperature effects in the perpendicular plane, the guiding center distribution is assumed as $f = F(v_\parallel,\mathbf{x},t)\delta(\mathbf{v}_\perp - \mathbf{v}_E)$, where $v_\perp$ denotes the velocity component perpendicular to the magnetic field, the relevant Vlasov–Poisson system reads [12]:

$$\frac{\partial F}{\partial t} + (\mathbf{v}_E + v_\parallel \mathbf{e}_z) \cdot \nabla F + \frac{e}{m}\mathbf{e}_z \cdot \nabla\varphi \frac{\partial F}{\partial v_\parallel} = 0,$$
$$\nabla^2 \varphi = 4\pi e n, \tag{6}$$

where $n(\mathbf{x}, t) = \int F \, dv_\parallel$.

In this paper, we present the newly developed particle-in-cell [13] (PIC) code MEP (acronym of Milano Electron Plasma [14]) for the solution of the system (6). In the literature, many electromagnetic [15–18] as well as electrostatic [19] 3D PIC codes are described. In the former case, the codes are usually relativistic [15,16,18] (in many case they are also strongly parallel [15–17]) and are often aimed to the study of relativistic beams or laser plasma interaction. The aim of the MEP code is to describe the behavior of the plasma in a cylindrical Penning trap. The code has to be flexible and fast enough to fit different experimental conditions. While many 2D PIC codes have been developed and successfully used (see, e.g. [20]), only few 3D PIC codes have been applied to such configurations [21]. Most of the existing codes, including those written especially for the case of non-neutral plasmas, are Cartesian [15,21], and/or adopt periodic boundary conditions, while the MEP code uses a cylindrical grid, which is more natural for the system under consideration; in particular, realistic and detailed boundary conditions can be easily imposed. There is also no need of a moving grid. In [19], e.g. the computational mesh fills a moving window and is laid down anew at each time step to describe the acceleration and transport of space-charge dominated beams in heavy ion inertial confinement fusion drivers. A "warped" Cartesian mesh is used to describe bends, and the Poisson's equation is solved with a 3D Fast Fourier Transform for the Cartesian part of the Laplacian operator (moving to the source term the non-Cartesian parts). In [21], the computation is done in a 3D Cartesian geometry (into which is embedded the confining cylinder) and the Poisson's equation is solved using a 3D multigrid algorithm. A particular mention deserves Delzanno et al. [22]: the geometry is cylindrical and compressional effects due to the finite size of the plasma column are retained including into the equations terms depending on the temperature and the effective plasma length (assumed as a function of the radial coordinate). In this case, some 3D effects are simply taken into account, although the numerical code remains 2D.

Being limited to the study of a strongly magnetized plasma, the MEP code solves the guiding center drift orbit equations, so it is faster than fully 3D codes, in which the shortest time scale to be resolved is the gyroperiod. This allows to follow the evolution of the system on a (relatively) long time even on a personal computer. The reason for this is also the use of a fast algorithm for the solution of the Poisson's equation (see Section 2.3). The length of the run depends of course in general mainly on the total number of grid points, the total number of macro-particles, the accuracy requested for solving Poisson's equation and the final (normalized) time. It depends also slightly on the chosen parameters (geometric and plasma parameters) and from the number of configuration savings. An adaptive time advancement scheme is employed: This is used to vary the step length automatically as the solution progresses, using small steps where the solution varies rapidly, and longer steps when changes are slow. The Courant condition ($\omega_p \Delta t < 1$) is in any case monitored to ensure that the code is numerically stable. It is therefore difficult to estimate in advance the total time duration of a single run. The test cases which are described in the paper were run on a personal computer with a 1.8 GHz processor and 512 MB RAM memory. The simulations shown in the paper lasted typically 24 h (CPU time). It is therefore practical to study the evolution of a trapped plasma to a state characterized by the (possible) presence of coherent structures. In particular, in the beam configuration case, an almost stationary state is reached with each run. To follow the "long-time" evolution of the coherent structures can become impractical on a desktop computer in the trapped plasma case, but on that time scale dissipative effects not included in the physical model may also begin to play a role. Finally, in the MEP code the problem is fully written in Hamiltonian form, so that the Liouville's theorem is satisfied by the numerical scheme. In addition, the energy conservation can be easily monitored (see Section 2.4). For a typical run with time-independent boundary conditions, the relative energy change is of the order of 10^{-5}.

The paper is organized as follows: the description of the MEP code is presented in Section 2; some characteristic results obtained for trapped plasmas and beams are discussed in Section 3; Section 4 is devoted to short conclusions and future developments of the code.

2. Description of the MEP code

2.1. Normalization of the equations

The evolution of the system is followed within a conducting cylindrical surface of radius R and length L on which the (in general time-dependent) boundary conditions for the electrostatic potential are imposed. Note that the system is determined by several geometrical and physical parameters: the magnetic field strength B; the sizes R, L and the geometry of the emitting surface; the potentials which are imposed on cathode, anode and drift tube; the initial electron velocity distribution and the initial current distribution emitted by the source. For example, Malmberg–Penning traps usually use a spiral-wound tungsten filament for the injection [14]. The MEP code is able to simulate this initial spatial distribution of the electrons; the effect of an accelerating grid is considered by suitably "cutting" the spiral along rows and columns of a given width. In addition, the code is able to take into account various initial velocity and current density distributions.

In the following, dimensionless quantities are used. Length, time, density and potential are normalized to R, $\omega_c/2\omega_p^2$, n_0 and $4\pi e n_0 R^2$, respectively, where ω_p is computed for a specified electron density n_0. Keeping the same notation for the normalized quantities, Eq. (6) is rewritten as:

$$\begin{aligned} &\frac{\partial F}{\partial t} + \left(\frac{1}{2}\mathbf{e}_z \times \nabla\varphi + v_\parallel \mathbf{e}_z\right) \cdot \nabla F + \frac{1}{M_{\text{eff}}}\mathbf{e}_z \cdot \nabla\varphi \frac{\partial F}{\partial v_\parallel} = 0, \\ &\nabla^2\varphi = n \end{aligned} \tag{7}$$

with $n = \int F \, \mathrm{d}v_\parallel$. For a given geometry and an initial plasma distribution, the behavior of the system is, therefore, characterized by the single parameter M_{eff}, which plays the role of an effective mass,

$$M_{\text{eff}} \equiv 4\omega_p^2/\omega_c^2 \simeq 4.115 \times 10^{-4} \frac{n_0 \ [10^7 \ \text{cm}^{-3}]}{B^2 \ [\text{kG}]}. \tag{8}$$

This gives $M_{\text{eff}} = 2n_0/n_B$, n_B being the so-called Brillouin density, $n_B \equiv (B^2/8\pi)/mc^2$, so that $0 \leqslant M_{\text{eff}} \leqslant 2$. In the beam configuration and again for a given geometry and an initial spatial distribution of the beam, at least an additional parameter is required to describe the system. This can be chosen, e.g. as the injected current I (assumed to be normalized to the ratio between $e\pi R^2 L n_0$ and the normalization time).

Using the variable $s \equiv r^2$, the equations of motion corresponding to the trajectories of the kinetic equation in (7), are:

$$\begin{aligned} &\frac{\mathrm{d}s}{\mathrm{d}t} = -\frac{\partial\varphi}{\partial\theta}, \\ &\frac{\mathrm{d}\theta}{\mathrm{d}t} = \frac{\partial\varphi}{\partial s}, \\ &\frac{\mathrm{d}z}{\mathrm{d}t} = v_\parallel, \\ &\frac{\mathrm{d}v_\parallel}{\mathrm{d}t} = \frac{1}{M_{\text{eff}}}\frac{\partial\varphi}{\partial z}. \end{aligned} \tag{9}$$

2.2. Mesh

In the MEP code, Eq. (7) is discretized on an equispaced grid (with the only exception of the radial cell around the cylindrical axis) in the coordinates s, θ and z. The number of grid cells is denoted as N_s, N_θ and N_z, respectively. In principle, N_θ and N_z can be arbitrary but the Fast Fourier Transform used for the solution of the Poisson equation (see below) works faster when these grid numbers are powers of two.

The grid for s is defined as $\underline{s}_0 = 0$, $\underline{s}_1 = 1/(N_s N_\theta + 1)$, $\underline{s}_{j+1} = \underline{s}_j + N_\theta/(N_s N_\theta + 1)$, $s_0 = 0$, $s_j = (\underline{s}_j + \underline{s}_{j+1})/2$, $j = 1,\ldots,N_s$ (s is the position of the center, while $\underline{s}$ denotes the lower boundary of a "radial" cell).

The grid for the azimuthal angle θ is simply $\theta_l = 2\pi(l-1)/N_\theta$, $l = 1,\ldots,N_\theta$, with the periodicity relation, $\theta_{N_\theta+1} = \theta_1$. Note in particular that the central cell has no subdivisions in θ.

Finally, the grid for the axial coordinate z is defined as $z_k = (k - 1/2)L/N_z - L/2$, $k = 1,\ldots,N_z$.

Each cell has the same volume $\Delta V = \Delta s \Delta\theta \Delta z/2$, with $\Delta s = 1/(N_s + 1/N_\theta)$, $\Delta\theta = 2\pi/N_\theta$, and $\Delta z = L/N_z$, respectively.

2.3. 3D Poisson equation solver

Using the coordinates (s,θ,z), the Poisson equation is written as

$$4\frac{\partial}{\partial s}s\frac{\partial\varphi}{\partial s} + \frac{1}{s}\frac{\partial^2\varphi}{\partial\theta^2} + \frac{\partial^2\varphi}{\partial z^2} = n, \tag{10}$$

$\varphi|_{s=1} = \breve{\varphi}(\theta,z)$ and $\varphi|_{z=\pm L/2} = \breve{\varphi}^{\pm}(s,\theta)$ represent the boundary conditions (possibly time-dependent).

A three-point finite differencing is applied to Eq. (10) on the above defined grid

$$n_{j,l,k} = \frac{4\underline{s}_{j+1}}{\Delta s^2}\left(\varphi_{j+1,l,k} - \varphi_{j,l,k}\right) - \frac{4\underline{s}_j}{\Delta s^2}\left(\varphi_{j,l,k} - \varphi_{j-1,l,k}\right) + \frac{1}{s_j\Delta\theta^2}\left(\varphi_{j,l-1,k} - 2\varphi_{j,l,k} + \varphi_{j,l+1,k}\right) + \frac{1}{\Delta z^2}\left(\varphi_{j,l,k-1} - 2\varphi_{j,l,k} + \varphi_{j,l,k+1}\right) \tag{11}$$

for $1 < j < N_s$ and $1 < k < N_z$. For $j = 0$ and $j = 1$, the equations are written as:

$$n_{0,k} = \frac{4\xi}{s_1 - s_0}\left(\frac{1}{N_\theta}\sum_{l=1}^{N_\theta}\varphi_{1,l,k} - \varphi_{0,k}\right) + \frac{1}{\Delta z^2}\left(\varphi_{0,k-1} - 2\varphi_{0,k} + \varphi_{0,k+1}\right), \tag{12}$$

$$n_{1,l,k} = \frac{4\underline{s}_2}{\Delta s^2}\left(\varphi_{2,l,k} - \varphi_{1,l,k}\right) - \frac{4\xi\underline{s}_1}{\Delta s(s_1 - s_0)}\left(\varphi_{1,l,k} - \varphi_{0,k}\right) + \frac{1}{s_1\Delta\theta^2}\left(\varphi_{1,l-1,k} - 2\varphi_{1,l,k} + \varphi_{1,l+1,k}\right) + \frac{1}{\Delta z^2}\left(\varphi_{1,l,k-1} - 2\varphi_{1,l,k} + \varphi_{1,l,k+1}\right) \tag{13}$$

(the numerical factor ξ is defined below), while for $j = N_s$ it results

$$n_{N_s,l,k} = \frac{8}{\Delta s^2}\left(\breve{\varphi}_{l,k} - \varphi_{N_s,l,k}\right) - \frac{4\underline{s}_{N_s}}{\Delta s^2}\left(\varphi_{N_s,l,k} - \varphi_{N_{s-1},l,k}\right) + \frac{1}{s_{N_s}\Delta\theta^2}\left(\varphi_{N_s,l-1,k} - 2\varphi_{N_s,l,k} + \varphi_{N_s,l+1,k}\right) + \frac{1}{\Delta z^2}\left(\varphi_{N_s,l,k-1} - 2\varphi_{N_s,l,k} + \varphi_{N_s,l,k+1}\right). \tag{14}$$

In Eq. (13) and in the following, s_0 is kept for the sake of generality. Finally, at the two circular bases ($k = 1, N_z$), one obtains:

$$n_{j,l,1} = \frac{4\underline{s}_{j+1}}{\Delta s^2}\left(\varphi_{j+1,l,1} - \varphi_{j,l,1}\right) - \frac{4\underline{s}_j}{\Delta s^2}\left(\varphi_{j,l,1} - \varphi_{j-1,l,1}\right) + \frac{1}{s_j \Delta\theta^2}\left(\varphi_{j,l-1,1} - 2\varphi_{j,l,1} + \varphi_{j,l+1,1}\right) + \frac{1}{\Delta z^2}\left(2\breve{\varphi}^-_{j,l} - 3\varphi_{j,l,1} + \varphi_{j,l,2}\right), \tag{15}$$

$$n_{j,l,N_z} = \frac{4\underline{s}_{j+1}}{\Delta s^2}\left(\varphi_{j+1,l,N_z} - \varphi_{j,l,N_z}\right) - \frac{4\underline{s}_j}{\Delta s^2}\left(\varphi_{j,l,N_z} - \varphi_{j-1,l,N_z}\right) + \frac{1}{s_j \Delta\theta^2}\left(\varphi_{j,l-1,N_z} - 2\varphi_{j,l,N_z} + \varphi_{j,l+1,N_z}\right) + \frac{1}{\Delta z^2}\left(\varphi_{j,l,N_z-1} - 3\varphi_{j,l,N_z} + 2\breve{\varphi}^+_{j,l}\right). \tag{16}$$

These relations can be cast in a matrix form, $\breve{\mathbf{n}} = -\hat{A}\boldsymbol{\varphi}$, or as

$$\breve{n}_{j,l,k} = -A_{j,l,k;\tilde{j},\tilde{l},\tilde{k}}\varphi_{\tilde{j},\tilde{l},\tilde{k}}, \tag{17}$$

where $\breve{\mathbf{n}}$ differs from $\mathbf{n}$ only in the boundary cells: here the definition of the density is modified to take explicitly into account the boundary conditions for $\boldsymbol{\varphi}$:

$$\begin{aligned}
&\breve{n}_{j,l,k} \equiv n_{j,l,k}, \quad j < N_s, \quad 1 < k < N_z,\\
&\breve{n}_{j,l,1} \equiv n_{j,l,1} - 2\breve{\varphi}^-_{j,l}/\Delta z^2, \quad j < N_s,\\
&\breve{n}_{j,l,N_z} = n_{j,l,N_z} - 2\breve{\varphi}^+_{j,l}/\Delta z^2, \quad j < N_s,\\
&\breve{n}_{N_z,l,k} \equiv n_{N_z,l,k} - 8\breve{\varphi}_{l,k}/\Delta s^2, \quad 1 < k < N_z,\\
&\breve{n}_{N_s,l,1} \equiv n_{N_s,l,1} - 2\breve{\varphi}^-_{N_s,l}/\Delta z^2 - 8\breve{\varphi}_{l,1}/\Delta s^2,\\
&\breve{n}_{N_s,l,N_z} = n_{N_s,l,N_z} - 2\breve{\varphi}^+_{N_s,l}/\Delta z^2 - 8\breve{\varphi}_{l,N_z}/\Delta s^2.
\end{aligned} \tag{18}$$

Analyzing Eqs. (11)–(16), it can be shown that the operator $\hat{A}$ is self-adjoint, i.e., $A_{j,l,k;\tilde{j},\tilde{l},\tilde{k}} = A_{\tilde{j},\tilde{l},\tilde{k};j,l,k}$. In addition, $\hat{A}$ is positively defined and commutative with the rotation operator, $(\hat{R}\varphi)_{j,l,k} \equiv (1-\delta\theta)\varphi_{j,l,k} + \delta\theta\varphi_{j,l+1,k}$, i.e., $\hat{R}\hat{A} = \hat{A}\hat{R}$.

Formally, the solution of the Poisson equation is $\boldsymbol{\varphi} = -\hat{A}^{-1}\breve{\mathbf{n}}$, where the inverse matrix $\hat{A}^{-1}$ have to be calculated only once. But the multiplication by the matrix $\hat{A}^{-1}$ requires a number of operations proportional to N_c^2, where $N_c \equiv N_s N_\theta N_z$ is the total number of grid cells. A more efficient algorithm is introduced. The Poisson's equation is Fourier transformed both in the azimuthal and in the axial coordinate. The computational grid is duplicated in the axial direction, the system is made periodic in z, and a standard Fast Fourier Transform (FFT) is applied, so that a set of one-dimensional differential equations in the radial coordinate are solved. Inverse FFT is then applied to get the solution on the grid.

More explicitly, potential and density are analyzed in Fourier series:

$$\begin{aligned}
\varphi_{j,l,k} &= \sum_{m_\theta=1-N_\theta/2}^{N_\theta/2}\sum_{m_z=1-N_z}^{N_z}\tilde{\varphi}_{j,m_\theta,m_z}\exp\left\{2\pi\mathrm{i}\left[\frac{m_\theta(l-1)}{N_\theta} + \frac{m_z(k-1)}{2N_z}\right]\right\},\\
\varphi_{0,k} &= \sum_{m_z=1-N_z}^{N_z}\tilde{\varphi}_{0,0,m_z}\exp\left[2\pi\mathrm{i}\frac{m_z(k-1)}{2N_z}\right],
\end{aligned} \tag{19}$$

$$\begin{aligned}
\breve{n}_{j,l,k} &= \sum_{m_\theta=1-N_\theta/2}^{N_\theta/2}\sum_{m_z=1-N_z}^{N_z}\tilde{n}_{j,m_\theta,m_z}\exp\left\{2\pi\mathrm{i}\left[\frac{m_\theta(l-1)}{N_\theta} + \frac{m_z(k-1)}{2N_z}\right]\right\},\\
\breve{n}_{0,k} &= \sum_{m_z=1-N_z}^{N_z}\tilde{n}_{0,0,m_z}\exp\left[2\pi\mathrm{i}\frac{m_z(k-1)}{2N_z}\right].
\end{aligned} \tag{20}$$

In this representation, the number of Fourier complex amplitudes is larger than the number of points in the grid, and additional conditions have to be imposed. Namely, the Fourier amplitudes satisfy the relations:

$$\tilde{n}_{j,m_\theta,m_z} = \tilde{n}^*_{j,-m_\theta,-m_z}, \quad \tilde{\varphi}_{j,m_\theta,m_z} = \tilde{\varphi}^*_{j,-m_\theta,-m_z},$$
$$\tilde{n}_{j,m_\theta,m_z} = -\tilde{n}_{j,m_\theta,-m_z}\exp(\pi i m_z/N_z), \quad \tilde{\varphi}_{j,m_\theta,m_z} = -\tilde{\varphi}_{j,m_\theta,-m_z}\exp(\pi i m_z/N_z).$$

The former relation is simply the reality condition for φ and $\breve{n}$, while the latter assures that the same relation is obtained between every Fourier amplitudes $\tilde{\varphi}_{j,m_\theta,m_z}$ and $\breve{n}_{j,l,k}$, including the boundary components with $k = 1$ and $k = N_z$. Namely, these conditions make the Fourier transforms of the z-boundary equations (16) identical with the transform of Eq. (11). Using Eqs. (19) and (20) in Eqs. (11)–(16) one obtains for $1 < j < N_s$

$$\tilde{n}_{j,m_\theta,m_z} = \frac{4\underline{s}_{j+1}}{\Delta s^2}\left(\tilde{\varphi}_{j+1,m_\theta,m_z} - \tilde{\varphi}_{j,m_\theta,m_z}\right) - \frac{4\underline{s}_j}{\Delta s^2}\left(\tilde{\varphi}_{j,m_\theta,m_z} - \tilde{\varphi}_{j-1,m_\theta,m_z}\right) - \frac{4\sin^2(m_\theta\Delta\theta/2)}{s_j\Delta\theta^2}\tilde{\varphi}_{j,m_\theta,m_z} - \frac{4\sin^2(m_z\pi\Delta z/2L)}{\Delta z^2}\tilde{\varphi}_{j,m_\theta,m_z} \tag{21}$$

or

$$\tilde{n}_{j,m_\theta,m_z} = \alpha_{j,m_\theta,m_z}\varphi_{j-1,m_\theta,m_z} + \beta_{j,m_\theta,m_z}\varphi_{j,m_\theta,m_z} + \gamma_{j,m_\theta,m_z}\varphi_{j+1,m_\theta,m_z} \tag{22}$$

with:

$$\alpha_{j,m_\theta,m_z} = \frac{4\underline{s}_j}{\Delta s^2},$$
$$\beta_{j,m_\theta,m_z} = -4\left[\frac{\underline{s}_{j+1}+\underline{s}_j}{\Delta s^2} + \frac{\sin^2(m_\theta\Delta\theta/2)}{s_j\Delta\theta^2} + \frac{\sin^2(m_z\pi\Delta z/2L)}{\Delta z^2}\right], \tag{23}$$
$$\gamma_{j,m_\theta,m_z} = \frac{4\underline{s}_{j+1}}{\Delta s^2}.$$

For $j = 0$, according to the first relation in Eq. (13), the coefficients are:

$$\alpha_{0,0,m_z} = 0,$$
$$\beta_{0,0,m_z} = -4\left[\frac{\xi}{s_1 - s_0} + \frac{\sin^2(m_z\pi\Delta z/2L)}{\Delta z^2}\right], \tag{24}$$
$$\gamma_{0,0,m_z} = \frac{4\xi}{s_1 - s_0}.$$

For $j = 1$, Eq. (13) gives:

$$\alpha_{1,0,m_z} = \frac{4\xi\underline{s}_1}{\Delta s(s_1 - s_0)}, \qquad \alpha_{1,m_\theta,m_z} = 0, \quad m_\theta \neq 0,$$
$$\beta_{1,m_\theta,m_z} = -4\left[\frac{\underline{s}_2}{\Delta s^2} + \frac{\xi\underline{s}_1}{\Delta s(s_1 - s_0)} + \frac{\sin^2(m_\theta\Delta\theta/2)}{s_1\Delta\theta^2} + \frac{\sin^2(m_z\pi\Delta z/2L)}{\Delta z^2}\right], \tag{25}$$
$$\gamma_{1,m_\theta,m_z} = \frac{4\underline{s}_2}{\Delta s^2},$$

while for $j = N_s$, Eq. (14) gives:

$$\begin{aligned}
&\alpha_{N_s,m_\theta,m_z} = \frac{4\underline{s}_{N_s}}{\Delta s^2},\\
&\beta_{N_s,m_\theta,m_z} = -4\left[\frac{2+\underline{s}_{N_s}}{\Delta s^2} + \frac{\sin^2(m_\theta\Delta\theta/2)}{s_{N_s}\Delta\theta^2} + \frac{\sin^2(m_z\pi\Delta z/2L)}{\Delta z^2}\right],\\
&\gamma_{N_s,m_\theta,m_z} = 0.
\end{aligned} \tag{26}$$

The solution is then found by means of a standard Gauss elimination procedure:

$$\begin{aligned}
&\tilde{n}_{j,m_\theta,m_z} = \tilde{\beta}_{j,m_\theta,m_z}\tilde{\varphi}_{j,m_\theta,m_z} + \gamma_{j,m_\theta,m_z}\tilde{\varphi}_{j+1,m_\theta,m_z},\\
&\tilde{\beta}_{j,m_\theta,m_z} \equiv \beta_{j,m_\theta,m_z} + \tilde{\alpha}_{j,m_\theta,m_z}\gamma_{j-1,m_\theta,m_z}, \quad \tilde{\alpha}_{j,m_\theta,m_z} \equiv -\frac{\alpha_{j,m_\theta,m_z}}{\tilde{\beta}_{j-1,m_\theta,m_z}},\\
&\tilde{\tilde{n}}_{j,m_\theta,m_z} \equiv \tilde{n}_{j,m_\theta,m_z} + \tilde{\alpha}_{j,m_\theta,m_z}\tilde{\tilde{n}}_{j-1,m_\theta,m_z},\\
&\tilde{\varphi}_{j,m_\theta,m_z} = \frac{1}{\tilde{\beta}_{j,m_\theta,m_z}}\tilde{\tilde{n}}_{j,m_\theta,m_z} - \frac{\gamma_{j,m_\theta,m_z}}{\tilde{\beta}_{j,m_\theta,m_z}}\tilde{\varphi}_{j+1,m_\theta,m_z}.
\end{aligned} \tag{27}$$

Inverse Fast Fourier Transform is then applied to get the solution on the grid. With this algorithm there is no need of matrix inversion and the Poisson's equation is solved with a number of operations proportional to $N_c\ln(N_\theta N_z)$.

2.4. Hamiltonian formulation

The system governed by Eq. (7) is simulated as an ensemble of macro-particles with fixed sizes Δs, $\Delta\theta$ and Δz, using a particle-in-cell method. Let the total number of macro-particles be N_p and let the αth macro-particle be characterized by the position $s_\alpha, \theta_\alpha, z_\alpha$ and the z-momentum p_α. It is assumed that the macro-particle gives a contribution $w_{j,l,k;\alpha}N_c/N_p$ to the electron density $n_{j,l,k}$ in the cell $\{j,l,k\}$. The weight functions $w_{j,l,k;\alpha}(s_\alpha,\theta_\alpha,z_\alpha)$ satisfy the condition $\sum_{j,l,k} w_{j,l,k;\alpha} = 1$, which provides the normalization of the particle density n and the charge conservation. The same weight functions are used for the computation of the potential corresponding to the particle position, $\varphi_\alpha(s_\alpha,\theta_\alpha,z_\alpha) = \sum_{j,l,k} w_{j,l,k;\alpha}(\varphi^0_{j,l,k} + \varphi^{\mathrm{vac}}_{j,l,k})$, where $\varphi^0_{j,l,k}$ is the solution of the Poisson equation with zero boundary conditions and $\varphi^{\mathrm{vac}}_{j,l,k}$ is the vacuum potential in the cell corresponding to the solution of the Laplace equation, $\nabla^2\varphi^{\mathrm{vac}} = 0$ with the given boundary conditions $\breve{\varphi}$ and $\breve{\varphi}^{\pm}$. The equations of motion corresponding to Eq. (9) can be written in Hamiltonian form, using the "momenta" s_α, p_α and the corresponding conjugated variables θ_α, z_α. The Hamiltonian function is written as:

$$H(\mathbf{s},\mathbf{p};\theta,\mathbf{z}) = \sum_\alpha \frac{p_\alpha^2}{2M_{\mathrm{eff}}} + U(\mathbf{s},\theta,\mathbf{z}), \tag{28}$$

$$\begin{aligned}
U &= -\frac{1}{2}\sum_\alpha\sum_{j,l,k} w_{j,l,k;\alpha}\varphi^0_{j,l,k} - \sum_\alpha\sum_{j,l,k} w_{j,l,k;\alpha}\varphi^{\mathrm{vac}}_{j,l,k}\\
&= \frac{1}{2}\sum_\alpha\sum_{j,l,k}\sum_{j',l',k'} w_{j,l,k;\alpha}A^{-1}_{j,l,k;j',l',k'}n_{j',l',k'} - \sum_\alpha\sum_{j,l,k} w_{j,l,k;\alpha}\varphi^{\mathrm{vac}}_{j,l,k}\\
&= \frac{N_c}{2N_p}\sum_{\alpha,\beta}\sum_{j,l,k}\sum_{j',l',k'} w_{j,l,k;\alpha}A^{-1}_{j,l,k;j',l',k'}w_{j',l',k,t;\beta} - \sum_\alpha\sum_{j,l,k} w_{j,l,k;\alpha}\varphi^{\mathrm{vac}}_{j,l,k}.
\end{aligned} \tag{29}$$

To obtain the equations of motion one has to calculate the derivatives $\partial H/\partial\zeta_\alpha$, where ζ_α is either s_α, or θ_α or z_α. Since the matrix $\hat{A}^{-1}$ is self-adjoint, the derivatives of the Hamiltonian for the equations of motion can

be calculated as $\partial H/\partial\zeta_\alpha = -\partial\varphi_\alpha/\partial\zeta_\alpha$. The equations of motion for the computational particles are solved in the code by means of the Runge–Kutta–Fehlberg predictor–corrector scheme [23].

Piecewise quadratic weight functions which are continuous with their first derivative are used:

$$\begin{aligned} w_{j,l,k;\alpha}(s_\alpha,\theta_\alpha,z_\alpha) &= W\left(\frac{s_\alpha - s_j}{\Delta s}\right) W\left(\frac{\theta_\alpha-\theta_l}{\Delta\theta}\right) W\left(\frac{z_\alpha - z_k}{\Delta z}\right) \quad \text{for } j>1,\\ w_{1,l,k;\alpha}(s_\alpha,\theta_\alpha,z_\alpha) &= W_1\left(\frac{s_\alpha - s_1}{\Delta s}\right) W\left(\frac{\theta_\alpha-\theta_l}{\Delta\theta}\right) W\left(\frac{z_\alpha - z_k}{\Delta z}\right),\\ w_{0,k;\alpha}(s_\alpha,\theta_\alpha,z_\alpha) &= W_0\left(\frac{s_\alpha - s_0}{\Delta s}\right) W\left(\frac{z_\alpha - z_k}{\Delta z}\right) \end{aligned} \tag{30}$$

with:

$$W(x) = \begin{cases} \frac{3}{4} - x^2, & |x| \leqslant 1/2,\\ \frac{1}{2}\left(\frac{3}{2} - |x|\right)^2, & 1/2 \leqslant |x| \leqslant 3/2,\\ 0, & |x| \geqslant 3/2, \end{cases} \tag{31}$$

$$W_1(x) = \begin{cases} 1 + \frac{2x}{1+2\underline{s}_1/\Delta s}, & x \leqslant -1/2,\\ \frac{3}{4} - x^2 - \frac{1-2\underline{s}_1/\Delta s}{2+4\underline{s}_1/\Delta s}\left(x-\frac{1}{2}\right)^2, & |x| \leqslant 1/2,\\ \frac{1}{2}\left(x-\frac{3}{2}\right)^2, & 1/2 \leqslant x \leqslant 3/2,\\ 0, & x \geqslant 3/2, \end{cases} \tag{32}$$

$$W_0(x) = \begin{cases} 1 - \frac{2x}{1+2\underline{s}_1/\Delta s}, & x \leqslant \underline{s}_1/\Delta s,\\ \frac{1}{1+2\underline{s}_1/\Delta s}\left(x - 1 - \frac{\underline{s}_1}{\Delta s}\right)^2, & \underline{s}_1/\Delta s \leqslant x \leqslant 1 + \underline{s}_1/\Delta s,\\ 0, & x \geqslant 1 + \underline{s}_1/\Delta s. \end{cases} \tag{33}$$

Note that as long as a sufficient number of macro-particles is used in the simulation (every cell occupied by the plasma should contain at least some macro-particles), this charge assignment scheme introduces little numerical noise.

If the space is filled by macro-particles with a uniform density, then all cells with $j > 1$ get a density $n_{j,l,k} \equiv \sum_\alpha w_{j,l,k;\alpha} N_c/N_p = 1$ (here it is taken into account that the cell volume is $\Delta s\Delta\theta\Delta z/2$, with $\Delta s = N_\theta/(N_s N_\theta + 1)$, $\Delta\theta = 2\pi/N_\theta$, $\Delta z = L/N_z$ and the weight function is integrated over this volume). For $j = 0$, 1, the integration gives

$$n_{0,k} = \frac{N_\theta/3 + 1 + 1/N_\theta}{1 + 2/N_\theta}, \quad n_{1,l,k} = (N_\theta + 1 - n_{0,k})/N_\theta \tag{34}$$

(here it is taken into account that $\underline{s}_1 = \Delta s/N_\theta$).

With these densities, Eqs. (11) and (13) are satisfied by:

$$\begin{aligned} \varphi_{j,l,k} &= C + \frac{s_j}{4} = C + \frac{\Delta s}{4}\left(j - \frac{1}{2} + \frac{1}{N_\theta}\right) \quad \text{if } j>1,\\ \varphi_{1,l,k} &= C + \frac{s_2}{4} - \Delta s\frac{N_\theta n_{1,l,k} + n_{0,k}}{4(N_\theta+1)} = \varphi_{2,l,k} - \frac{\Delta s}{4},\\ \varphi_{0,k} &= \varphi_{1,l,k} - n_{0,k}\frac{s_1 - s_0}{4\xi} = \varphi_{1,l,k} - \frac{\Delta s}{8\xi}\left(\frac{N_\theta}{3} + 1 - \frac{1}{N_\theta}\right). \end{aligned} \tag{35}$$

For a macro-particle with $s_\alpha \geqslant \underline{s}_2$ this gives a linear potential,

$$\varphi_\alpha \equiv \sum_{j,l,k} \varphi_{j,l,k} w_{j,l,k;\alpha} = C + \frac{s_\alpha}{4}, \tag{36}$$

while for a particle with $s_\alpha < \underline{s}_2$ it results

$$\begin{aligned}\varphi_\alpha &= \frac{s_\alpha}{4\xi(1+2/N_\theta)}\left(\frac{N_\theta}{3}+1-\frac{1}{N_\theta}\right) + \varphi_{1,j,k} - \frac{\Delta s}{8\xi}\left(\frac{N_\theta}{3}+1-\frac{1}{N_\theta}\right) \\ &= C + \frac{\Delta s}{4}\left(\frac{1}{2}+\frac{1}{N_\theta}\right) + \frac{1}{\xi(1+2/N_\theta)}\left(\frac{N_\theta}{3}+1-\frac{1}{N_\theta}\right)\left[\frac{s_\alpha}{4} - \frac{\Delta s}{4}\left(\frac{1}{2}+\frac{1}{N_\theta}\right)\right].\end{aligned} \tag{37}$$

In order to obtain the same linear dependence as in Eq. (36), one has to set

$$\xi = \frac{N_\theta/3 + 1 + 1/N_\theta}{1+2/N_\theta}. \tag{38}$$

To end up, note that in this Hamiltonian formulation of both the problem and the numerical scheme, the symmetry of $\hat{A}$ plays a fundamental role: It assures the conservation of phase integrals (Liouville's theorem) and the conservation of the energy in a problem with time-independent boundary conditions.

3. Results

The code has been used to simulate the plasma dynamics in a Malmberg–Penning trap for different possible experimental settings. The first case presented here refers to an electron plasma trapped in a potential well (Fig. 1, left), the radial confinement being guaranteed by the presence of a strong, axial magnetic field. With the three-dimensional code it is possible to investigate the limitations of the analogy between the bounce averaged electron motion and the 2D fluid motion, valid in the limit where the axial bounce frequency is much higher than the azimuthal rotation frequency. A case where the two frequencies are of the same order (low rigidity) is presented in Fig. 2, where it is shown that a plasma column initially set off-axis does not move rigidly perpendicularly to the axis, but is strongly distorted both axially and transversally.

As a second example, the experimentally relevant case of an electron beam injected in a drift tube is analyzed [14] (Figs. 3–5), which corresponds to the setting shown in Fig. 1, right. The electrons are generated from a cathode with an Archimedean spiral shape. The effect of the presence of an accelerating grid is simulated by suitably "cutting" the spiral along rows and columns of a given width. The drift tube is equipotential (grounded), but the exit section is maintained at a (strongly) positive potential, simulating the voltage used (see [14]) to accelerate the electrons against a phosphor screen, for their imaging. Fig. 3 represents the plasma density distribution at a given time (when stationary conditions have been already reached) in different slices transverse to the tube: the first close to the source, the last close to the collector. The time evolution of the emitted electrons is shown in Fig. 4, which refers to the axial phase space $(z,v_\parallel)$, and in Fig. 5, which represents the electron distribution in the (r,z) plane.

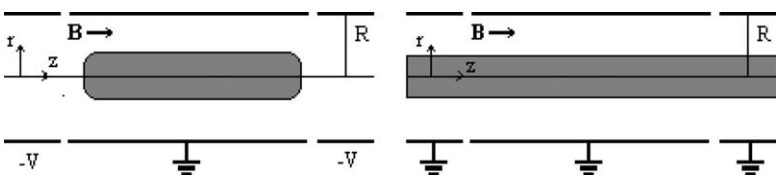

Fig. 1. Scheme of a trapped plasma configuration (left) and a travelling beam configuration (right). $-V$ is the trap potential.

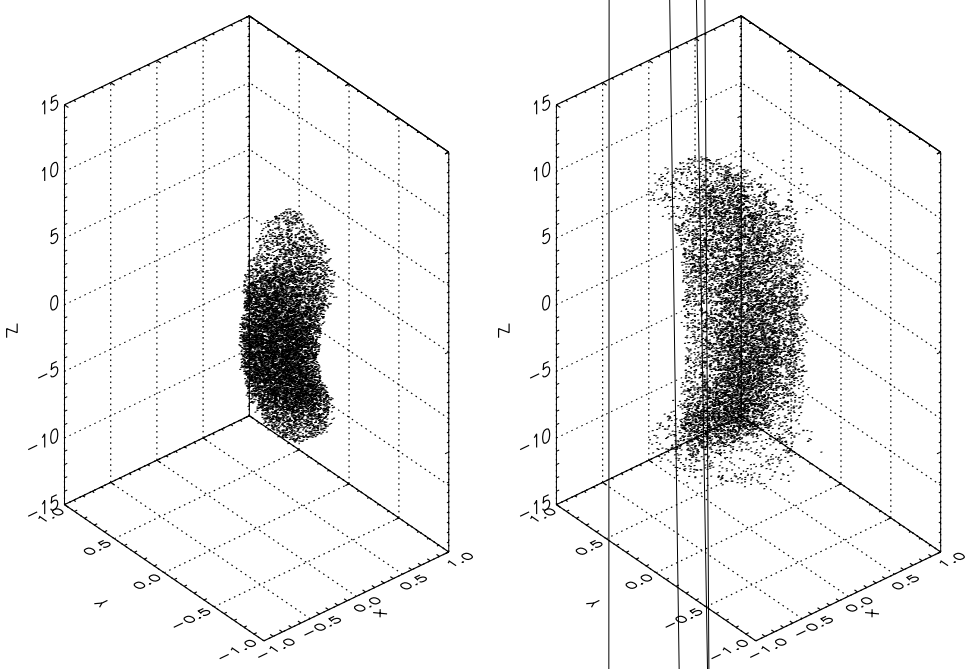

Fig. 2. 3D plot of the particle configuration, in the case of a trapped plasma, at $t = 1.0$ (left) and $t = 4.0$ (right). The parameters of the run are: $M_{\text{eff}} = 0.325$, $L/R = 22.222$, $N_s = 64$, $N_\theta = 64$, $N_z = 128$, $N_{\text{p}} = 10^5$. The initial configuration is that of a uniform electron column, centered at a distance 0.25 from the axis of the trap, with a radius 0.3, and located axially between $z = -1$ and $z = 1$. The plug potentials are -100. All quantities are dimensionless.

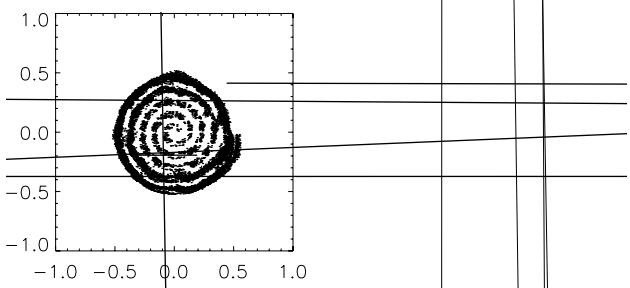

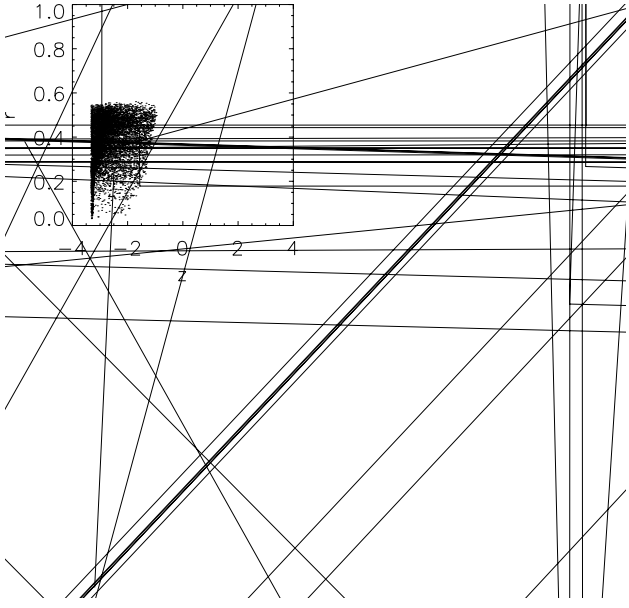

In particular, the formation of a ''virtual cathode'' close to the injection boundary is evidenced. The central part of the beam is reflected back to the cathode by the space-charge of the beam itself, and only the outer part of the beam reaches the opposite end of the trap, held at positive potential. The ''annular'' beam which travels to the collector shows a quasi-2D evolution of vortex structures. The simulation captures the essential physical processes found also in the experiments [10].

In almost stationary conditions, three regions can be distinguished: a reflection region close to the injection boundary, a central part with almost constant parallel velocity, and an acceleration region close to the exit boundary.

Finally, in Figs. 6–8 the case of a plasma filling the trap is studied; the conditions are similar to the previous case, but the exit section is held at a negative potential. This situation simulates the phase of injection of the electrons in a Malmberg–Penning trap. In this phase, the plug electrode at the end of

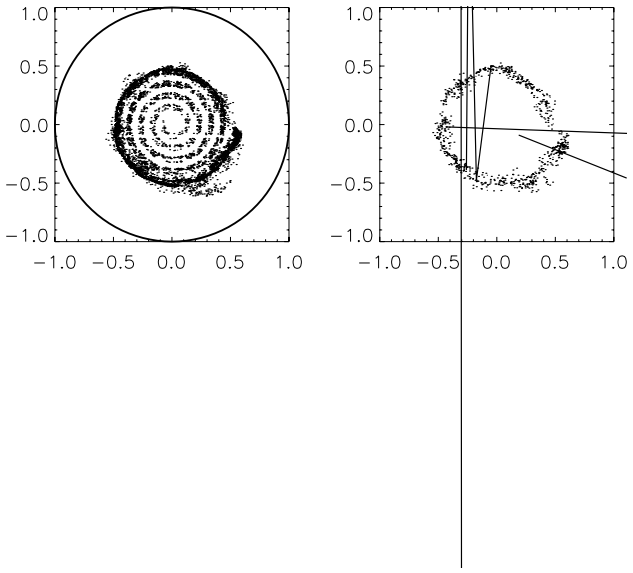

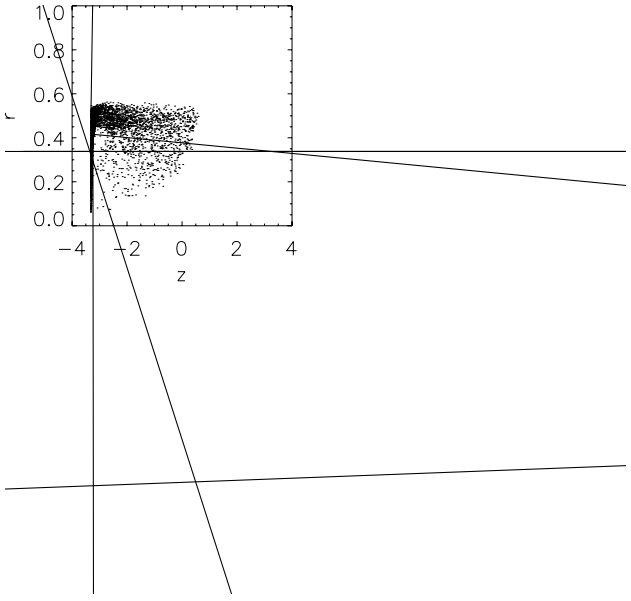

the trap is maintained at a sufficiently negative potential in order to reflect the electrons entering the trap, while the plug electrode at the entrance is grounded to let the electrons flow into the trap from the cathode (starting from this configuration, the trapping phase is obtained by simply lowering the plug potential at the entrance of the beam, to the same value as the end potential, so that the electrons are electrostatically trapped along the axis of the device). At low injection currents, one would usually expect the formation of an electron column with almost constant density, which fills the region between the two end sections of the cylindrical drift tube, with the maximum density increasing with the value of the plug potential, as it is confirmed by the simulations (not reported here). However, when the input current of the beam is further increased, new effects may take place. In particular, due to the space charge close to the entrance, some electrons can be reflected back to the cathode. Then, the charge cloud represents a barrier not only for the electrons which try to enter the trap, but also for the electrons which are reflected by the negative potential at the end of the trap itself. As a result, the electron plasma which fills the trap assumes an annular shape, as shown in Fig. 8.

4. Concluding remarks

We have shown that the MEP code gives a good description of the formation of spatial coherent structures observed in the experiments on electron plasmas trapped in a Malmberg–Penning trap with a highly uniform magnetic field. The code has been successfully used also to describe different processes occurring in a low-energy electron beam produced in the same configuration (in particular, the transition to a space charge dominated regime). The description of the system is based on a drift electrostatic approximation, which includes kinetic effects in the parallel motion. This allows to investigate phase space processes, as kinetic equilibria and the formation of holes and coherent structures. Possible modifications of the code concern its extension to the case of non-uniform magnetic field, and the inclusion of collisions.

References

[1] R.C. Davidson, An Introduction to the Physics of Nonneutral Plasmas, Addison-Wesley, Redwood City, USA, 1990.
[2] T.M. O'Neil, Trapped plasmas with a single sign of charge, Phys. Today 52 (2) (1999) 24.
[3] K.S. Fine, C.F. Driscoll, J.H. Malmberg, T.B. Mitchell, Measurements of symmetric vortex merger, Phys. Rev. Lett. 67 (1991) 588.
[4] T.B. Mitchell, C.F. Driscoll, Electron vortex orbits and merger, Phys. Fluid 8 (1996) 1828.
[5] K.S. Fine, A.C. Cass, W.G. Flynn, C.F. Driscoll, Relaxation of 2D turbulence to vortex crystals, Phys. Rev. Lett. 75 (1995) 3277.
[6] D.H.E. Dubin, T.M. O' Neil, Trapped nonneutral plasmas, liquids, and crystals (the thermal equilibrium states), Rev. Mod. Phys. 71 (1999) 87.
[7] C.F. Driscoll, J.H. Malmberg, K.S. Fine, Observation of transport to thermal equilibrium in pure electron plasmas, Phys. Rev. Lett. 60 (1988) 1290.
[8] A.J. Peurrung, J. Fajans, A limitation to the analogy between pure electron plasmas and two-dimensional inviscid fluids, Phys. Fluid B 5 (1993) 4295.
[9] J.W. Luginsland, Y.Y. Lau, R.J. Umstattd, J.J. Watrous, Beyond the Child–Langmuir law: a review of recent results on multidimensional space-charge-limited flow, Phys. Plasmas 9 (2002) 2371.
[10] G. Bettega, F. Cavaliere, A. Illiberi, R. Pozzoli, M. Romé, M. Cavenago, Yu. Tsidulko, Experimental investigations of coherent structures in a low-energy electron beam, Appl. Phys. Lett. 84 (2004) 3807.
[11] C.F. Driscoll, K.S. Fine, Experiments on vortex dynamics in pure electron plasmas, Phys. Fluid B 2 (1990) 1359.
[12] J.S. deGrassie, J.H. Malmberg, Waves and transport in the pure electron plasma, Phys. Fluid 23 (1980) 63.
[13] C.K. Birdsall, A.B. Langdon, Plasma Physics via Computer Simulation, Institute of Physics Publishing, Bristol, UK, 1991.
[14] M. Amoretti, G. Bettega, F. Cavaliere, M. Cavenago, F. De Luca, R. Pozzoli, M. Romé, Cylindrical penning trap for the study of electron plasmas, Rev. Sci. Instr. 74 (2003) 3991.
[15] A. Pukhov, Three-dimensional electromagnetic relativistic particle-in-cell code VLPL (Virtual Laser Plasma Lab), J. Plasma Phys. 61 (1999) 425.
[16] R.A. Fonseca, L.O. Silva, F.S. Tsung, V.K. Decyk, W. Lu, C. Ren, W.B. Mori, S. Deng, T. Katsouleas, J.C. Adam, OSIRIS: a three-dimensional, fully relativistic particle in cell code for modeling plasma based accelerators, in: P.M.A. Sloot, C.J. Kenneth Tan, J.J. Dongarra, A.G. Hoekstra (Eds.), Proceedings of the ICSS 2002 International Conference, Amsterdam, The Netherlands, vol. 2331, part III, Springer-Verlag, Heidelberg, Germany, 2002, p. 342.
[17] J. Wang, D. Kondrashov, P.C. Liewer, S.R. Karmesin, Three-dimensional deformable-grid electromagnetic particle-in-cell for parallel computers, J. Plasma Phys. 61 (1999) 367.
[18] J.P. Kuska, J. Büchner, The three-dimensional fully kinetic electromagnetic PIC simulation code GISMO, in: Proceedings of the Seventh International Conference on Plasma Astrophysics and Space Physics, Kluwer Academic Publishers, Dordrecht, 1999, p. 645.
[19] A. Friedman, D.P. Grote, I. Haber, Three-dimensional particle simulation of heavy-ion fusion beams, Phys. Fluid B 4 (1992) 2203.
[20] J.P. Varboncoeur, A.B. Langdon, N.T. Gladd, An object-oriented electromagnetic PIC code, Comput. Phys. Commun. 87 (1995) 199.
[21] G.W. Mason, R.L. Spencer, Simulations of the instability of the $m = 1$ self-shielding diocotron mode in finite-length non-neutral plasmas, Phys. Plasmas 9 (2002) 3217.
[22] G. Delzanno, G. Lapenta, J.M. Finn, KANDISKY: a PIC Code for fluid simulations of penning traps, IEEE Trans. Plasma Sci. 30 (2002) 34.
[23] G.E. Forsythe, M.A. Malcolm, C.B. Moler, Computer Methods for Mathematical Computations, Prentice-Hall, Englewood Cliffs, NJ, USA, 1977.